



Article scientifique

Article

2018

Published version

Open Access

This is the published version of the publication, made available in accordance with the publisher's policy.

---

## 4-D Imaging of Subsurface Changes with Coda Waves: Numerical Studies of 3-D Combined Sensitivity Kernels and Applications to the $M_w$ 7.9, 2008 Wenchuan Earthquake

---

Obermann, Anne; Planes, Thomas; Larose, Eric; Campillo, Michel

### How to cite


OBERMANN, Anne et al. 4-D Imaging of Subsurface Changes with Coda Waves: Numerical Studies of 3-D Combined Sensitivity Kernels and Applications to the  $M_w$  7.9, 2008 Wenchuan Earthquake. In: Pure and Applied Geophysics, 2018. doi: 10.1007/s00024-018-2014-7

This publication URL: <https://archive-ouverte.unige.ch/unige:115056>

Publication DOI: [10.1007/s00024-018-2014-7](https://doi.org/10.1007/s00024-018-2014-7)



## 4-D Imaging of Subsurface Changes with Coda Waves: Numerical Studies of 3-D Combined Sensitivity Kernels and Applications to the $M_w$ 7.9, 2008 Wenchuan Earthquake

ANNE OBERMANN,<sup>1</sup>  THOMAS PLANÈS,<sup>2</sup> ERIC LAROSE,<sup>3</sup> and MICHEL CAMPILLO<sup>3</sup>

**Abstract**—In the context of seismic monitoring, recent studies made successful use of seismic coda waves to image the lateral extent of medium changes. Locating the depth of the changes, however, remains a challenge. We use multiply scattered body- and surface-wave 3-D combined sensitivity kernels to address this problem. We show that we can locate velocity perturbations at depth with numerical data from elastic wave-field simulations in 3-D heterogeneous media. This procedure is then applied to assess the extent of the crustal damage due to the  $M_w$  7.9, 2008 Wenchuan earthquake. We discuss the potential and limitations of our approach to retrieve the depth information of temporal changes occurring in heterogeneous structures.

### 1. Introduction

The detection of temporal variations in the coda of repeating earthquakes or ambient seismic noise correlations has been successfully applied in different areas in seismology. This method allows monitoring of temporal changes occurring in various settings, such as oil and gas reservoirs (Meunier et al. 2001), CO<sub>2</sub> and geothermal fluid injection studies (Ugalde et al. 2013; Obermann et al. 2015; Hillers et al. 2015), volcanoes (Poupinet et al. 1996; Grêt et al. 2005; Sens-Schönfelder and Wegler 2006a), and fault zones (Poupinet et al. 1984; Schaff and Beroza 2004; Peng and Ben-Zion 2006; Wu et al. 2009; Takagi et al. 2012; Roux and Ben-Zion 2014).

Not only the temporal evolution of the changes is of interest, but also their spatial distribution within the medium, as well as their physical origin (subject to interpretation). Retrieving the spatial distribution

of the changes using coda waves is not a straightforward problem given the complexity of the multiply scattered wave paths. This is why coda waves measurements were initially limited to detection purposes only. However, Pacheco and Snieder (2005) showed that the phase shift of coda waves induced by a localized velocity change could be modelled using a 'statistical' sensitivity kernel. This kernel describes the proportion of scattered wave energy that interacts, on average, with the velocity change. Larose et al. (2010) and Rossetto et al. (2011) showed that a similar sensitivity kernel could describe the coda wave decoherence induced by a local scattering change (or structural change). The similarities and differences between these kernels are described in Planès et al. (2014) and Margerin et al. (2016). To retrieve the spatial distribution of the changes, a linear inverse problem can be solved. This was applied to numerical simulations (Planès 2013; Planès et al. 2015; Kanu and Snieder 2015b), locating precursors of volcanic eruptions (Obermann et al. 2013a; Lesage et al. 2014; Sanchez et al. 2018), assessing fault zone damages (Froment 2011; Obermann et al. 2014a), subsurface changes due to high-pressure fluid injections (Obermann et al. 2015; Hillers et al. 2015), and crack/fissure growth in concrete blocks (Larose et al. 2010, 2015; Zhang et al. 2016).

These kernels are based on the description of the wave propagation intensity in the scattering medium. In the aforementioned applications, the coda waves are assumed to be composed of a single propagation mode, either surface waves or body waves. This assumption allows use of analytical expressions of the multiply scattered intensity propagator. Hence, either a 2-D sensitivity kernel describing the 2-D surface wave intensity propagation, or a 3-D

<sup>1</sup> Swiss Seismological Service, ETH Zurich, Zurich, Switzerland. E-mail: anne.obermann@sed.ethz.ch

<sup>2</sup> Université de Genève, Geneva, Switzerland.

<sup>3</sup> ISTerre, CNRS, Université de Grenoble, Grenoble, France.

sensitivity kernel describing the 3-D body-wave intensity propagation is used. However, coda waves are composed of different propagation modes, namely,  $P$ ,  $S$  and surface waves, in proportions that depend on the degree of heterogeneity, coda lapse time, source mechanism, etc. (Perton et al. 2009; Margerin et al. 1999; Hennino et al. 2001; Obermann et al. 2013b). Building sensitivity kernels that describe the full complexity of the coda wave composition is not an easy task as the elastic radiative transfer equation does not even have an analytical solution for the half space. An interesting approach has been proposed by Kanu and Snieder (2015a), based on 2-D numerical simulations of the acoustic and elastic wave fields in heterogeneous media. This approach consists of computing the intensity propagator through an ensemble average of the envelope of the coda wave field obtained in different realisations of the disorder. This approach has the strong advantage of intrinsically taking into account all the complexity of the wave field (mode conversions, inhomogeneous velocity or scattering, topography, etc.). However, the computational cost of the 2-D acoustic simulations is high and the convergence to a stable solution slow. The approach has yet to be extended to 3-D and to an elastic wave propagation.

Another approach based on the linear combination of surface- and body-wave sensitivity kernels was proposed by Obermann et al. (2016). Obermann et al. (2016) have shown that a linear combination of the 2-D (surface wave) and 3-D (body wave) kernel describes well the sensitivity of the multiply scattered waves as a function of depth and lapse time in the coda. The downside is that this method (at the moment) can only describe the subsurface with uniform velocity and heterogeneity.

In the present paper, we show with wave-field simulations in 3-D multiply scattering media that a combination of body- and surface-wave 3-D sensitivity kernels (combined kernels) can indeed be used to constrain the depth location of medium changes. We first describe the combined kernels (Sect. 2.1) and the numerical wave-field simulations (Sect. 2.2). Then, imaging results obtained from numerical simulations with local velocity perturbations at various depths are shown (Sect. 3) and the potential and limitations of our approach are discussed. We then

apply the method to the  $M_w$  7.9, 2008 Wenchuan earthquake, to assess the extent of the crustal damage (Sect. 4).

## 2. Methods

### 2.1. Multiply Scattered Body- and Surface-Wave 3-D Combined Sensitivity Kernels

Pacheco and Snieder (2005) first described the sensitivity of acoustic coda waves to a velocity perturbation in a multiply scattering medium. The velocity change in the medium induces a relative phase shift in the coda waves that can be measured in the time or spectral domain as  $\varepsilon(t) = \frac{\delta t}{t}$ , where  $\delta t(t)$  is the phase shift and  $t$  is the lapse time in the coda (Sens-Schönfelder and Wegler 2006a). Pacheco and Snieder (2005) showed that the sensitivity of the coda depends on the position of the change relative to the source and receiver, the lapse time in the coda, and the strength of the velocity change. They introduced the following sensitivity kernel  $K$  to model the induced relative phase shifts  $\varepsilon$  at a lapse time  $t$  in the coda:

$$\varepsilon(t) = \frac{\delta V}{V} \frac{dv}{v} K, \quad (1)$$

where  $\delta V$  is the perturbation volume and  $\frac{dv}{v}$  the actual local velocity change. The sensitivity kernel  $K$  is defined as follows:

$$K(\mathbf{S}, \mathbf{R}, \mathbf{r}_0, t) = \frac{\int_0^t p(\mathbf{S}, \mathbf{r}_0, u) p(\mathbf{r}_0, \mathbf{R}, t - u) du}{p(\mathbf{S}, \mathbf{R}, t)}, \quad (2)$$

where  $\mathbf{S}$  and  $\mathbf{R}$  are the positions of the source and the receiver, respectively,  $\mathbf{r}_0$  is the position of the local velocity variation, and  $t$  is the centre of the time interval in the coda where the phase shifts are evaluated. Here,  $p(\mathbf{a}, \mathbf{b}, t)$  is the intensity propagator of the scattered wave field from  $\mathbf{a}$  to  $\mathbf{b}$  at time  $t$ . So far, most studies used the analytical solution of the acoustic isotropic radiative transfer equation (Paasschens 1997) or the solution of the diffusion equation for  $p$ . As discussed in the introduction, in more general and realistic scattering media (elastic, non-diffusive, anisotropically scattering), the intensity propagators would have to be computed numerically.

This same kernel was later shown to also describe the decorrelation of coda waves induced by a scattering perturbation (Larose et al. 2010; Rossetto et al. 2011; Planès et al. 2014). Note that this kernel is only valid in the diffusion regime, i.e. when the heterogeneity level is high enough to render the wave energy flux isotropic at the local variation position  $r_0$ . Outside the diffusion regime, a propagator including the direction of the flux needs to be used (i.e. the specific intensity, see Margerin et al. 2016).

Obermann et al. (2016) proposed to obtain 3-D combined sensitivity kernels that can describe the complexity of the coda, as a linear combination of 2-D surface ( $\varepsilon^{\text{Surf}}$ ) and 3-D body wave ( $\varepsilon^{\text{Body}}$ ) sensitivities:

$$\varepsilon(r_0, t) = \alpha(t)\varepsilon^{\text{Surf}}(r_0, t) + (1 - \alpha(t))\varepsilon^{\text{Body}}(r_0, t). \quad (3)$$

Here,  $\varepsilon(r_0, t)$  is the relative phase shift of coda waves measured at time  $t$  in the coda for a change/variation at position  $r_0$  in space.  $\varepsilon^{\text{Surf}}$  is the contribution of surface waves:

$$\varepsilon^{\text{Surf}}(r_0, t) = \frac{\delta V}{t} \frac{dv}{v} K^{\text{Surf}}(x_0, y_0, t) \Gamma(z_0), \quad (4)$$

and  $\varepsilon^{\text{Body}}$  is the contribution of body waves:

$$\varepsilon^{\text{Body}}(r_0, t) = \frac{\delta V}{t} \frac{dv}{v} K^{\text{Body}}(r_0, t). \quad (5)$$

In Eq. 4,  $\varepsilon^{\text{Surf}}$  is computed with a 2-D sensitivity kernel to describe lateral variations of the sensitivity of surface waves in the horizontal plane:

$$K^{\text{Surf}}(x_0, y_0, t) = \frac{\int P^{2D}(S, x_0, y_0, u) P^{2D}(x_0, y_0, R, t - u) du}{P^{2D}(S, R, t)}, \quad (6)$$

and multiplied by a 1-D depth sensitivity profile  $\Gamma(z_0)$  corresponding to the sensitivity of the fundamental mode of Rayleigh waves.

$\varepsilon^{\text{Body}}$  in Eq. 5 is computed using a 3-D kernel describing the sensitivity of an effective scattered body-wave mode:

$$K^{\text{Body}}(r_0, t) = \frac{\int P^{3D}(S, r_0, u) P^{3D}(r_0, R, t - u) du}{P^{3D}(S, R, t)}. \quad (7)$$

Following Planès et al. (2014), we use the 2-D and 3-D radiative transfer solution for isotropic scattering

(Paasschens 1997) to model the intensity transport of the surface ( $P^{2D}$ ) and body waves ( $P^{3D}$ ), respectively. With this formulation, we do not consider  $P$ - to  $S$ -mode conversions but describe  $P$  and  $S$  waves as a single effective mode with an effective speed  $c_E$ . We thus make the assumption of the diffusive regime (isotropic wave energy flux) implying the equipartition of the energy of different states of  $P$  and  $S$  waves in the coda (Weaver 1982, 1985). In a Poisson half-space, the theoretical energy ratio of  $S/P$  is 7.19 at the surface and 10.39 at depth (absence of surface waves; Hennino et al. 2001; Tregourès and van Tiggelen 2002). Obermann et al. (2016) observed an average ratio of  $\langle S^2 \rangle / \langle P^2 \rangle = 9 \pm 2$  for the simulations we are using here, implying a strong dominance of  $S$  waves over  $P$  waves. Using this ratio, the effective travel time of the waves  $t_E$  can be determined in a statistical way, as a linear combination of the time that the waves spend in each mode:

$$t_E = \frac{P}{P+S} t_P + \frac{S}{S+P} t_S. \quad (8)$$

The proportion of  $P$ -wave energy can be expressed as  $\frac{P}{P+S} = \frac{1}{1+x}$  and the proportion of  $S$ -wave energy can be expressed as  $\frac{S}{P+S} = \frac{x}{1+x}$ , with  $x = S/P = 9$ . Substituting travel times with velocities yields the effective velocity  $c_E$ :

$$\frac{1}{c_E} = \frac{0.1}{V_S} + \frac{0.9}{V_P}. \quad (9)$$

For the settings in these numerical simulations,  $c_E \approx 3.9$  km/s. The contribution of surface and body waves at different positions  $r_0$  and at each lapse time  $t$  in the coda is modelled with the lapse time-dependent partition coefficient  $\alpha$ . In this way, we take into account surface body wave conversions, as we allow the partition ratio to vary along time in the coda. Numerical simulations (Obermann et al. 2013b, 2016) have shown that the partition coefficient follows a universal behaviour with respect to the coda lapse time expressed in terms of the mean free time  $t^\star = \frac{\ell^\star}{c_E}$ . The mean free time depends on the degree of medium heterogeneity measured through the transport mean free path  $\ell^\star$  and the energy velocity  $c_E$ . Roughly speaking, the transport mean free path corresponds to the propagation distance after which the energy flux of the multiply scattered

waves becomes isotropic. Obermann et al. (2016) observed that the surface waves dominate the depth sensitivity for about eight mean free times, while the body waves dominate the depth sensitivity at later times.

The advantage of this approach of combining surface- and body-wave sensitivity is that no numerical wave-field simulation is required to construct the kernels. These kernels can, however, only represent the sensitivity in media described by a uniform velocity  $c_E$  and a uniform transport mean free path  $\ell^\star$ . Additionally, because of the approximation of the diffusive regime, these kernels might not realistically describe the coda sensitivity in low scattering regimes.

In Fig. 1, slices through the 3-D combined kernels are shown; two horizontal slices at different depth [0.5 km (a), 1.5 km (b)] and a vertical slice (c) along the position indicated with the red line in (a). We observe a sensitivity concentration along the source/receiver line as well as a large sensitivity at shallow depths (c).

## 2.2. Numerical Wave-Field Simulations

We perform numerical simulations of wave-field propagation in 3-D heterogeneous elastic media without intrinsic attenuation. We use SPECfEM3D for the simulations, which is based on a continuous Galerkin spectral element method (Komatitsch and Tromp 2002; Peter et al. 2011). The model size is  $10 \times 10 \times 6 \text{ km}^3$  in the  $x$ ,  $y$  and  $z$  directions, respectively. The grid spacing is  $\delta x = \delta y = \delta z = 50 \text{ m}$ . The

record length is 16 s with a time step of  $10^{-4} \text{ s}$ . For the heterogeneous medium, we use a von Karman distribution with a correlation length of  $a = 300 \text{ m}$ , which is in the order of one  $P$  wavelength ( $\lambda_P = 325 \text{ m}$ ), and consider velocity fluctuations of  $\sigma = 20\%$  around a background  $P$ -wave velocity of  $v_P = 6500 \text{ m/s}$ . The  $S$ -wave velocity depends on the  $P$ -wave velocity with  $v_S = v_P/\sqrt{3}$  ( $\lambda_S = 190 \text{ m}$ ). We use an isotropic source with a central frequency of 20 Hz at nine different positions (all combinations of  $x = 1, 5, 9 \text{ km}$  and  $y = 1, 5, 9 \text{ km}$ ) in the first grid point below the surface ( $z = 50 \text{ m}$ ). Receivers that measure vertical displacement are placed in a regular grid on the free surface with 100-m spacing. An example of this setup is shown in Fig. 2, with some selected receivers. The simulations follow the setup of Obermann et al. (2016), who determined the transport mean free path for these settings as  $\ell^\star = 1840 \text{ m}$  from the intensity of the recorded signals that was fitted with the diffusion equation (Margerin et al. 1999). Please note that the different wavelengths of  $P$  and  $S$  waves cause a different sampling of the scattering pattern and result in different mean free paths for  $P$  and  $S$  waves. Obermann et al. (2016) did not separate both wave types, but considered the effective scattering mean free path for the wave field as a whole, which is associated with the propagation speed of the energy of the mixture of the  $P$  and  $S$  waves; the effective velocity  $c_E$ .

For field data, the degree of heterogeneity can often be estimated; for instance, via the decay of the coda envelope (Margerin et al. 1999; Nakahara and Carcolé 2010), phase statistics (Obermann et al.

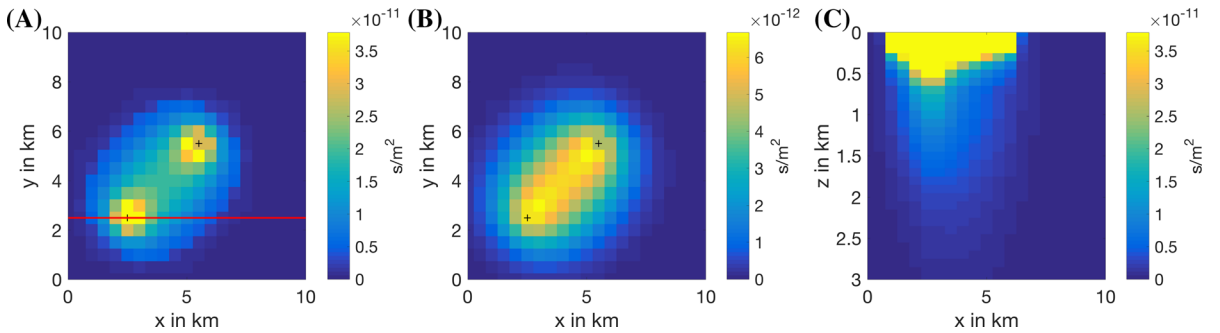


Figure 1

3-D combined kernels. Horizontal slices at depths of 0.5 km (a) and 1.5 km (b) and a vertical slice (c) along the red line indicated in a. The crosses mark the source and receiver positions

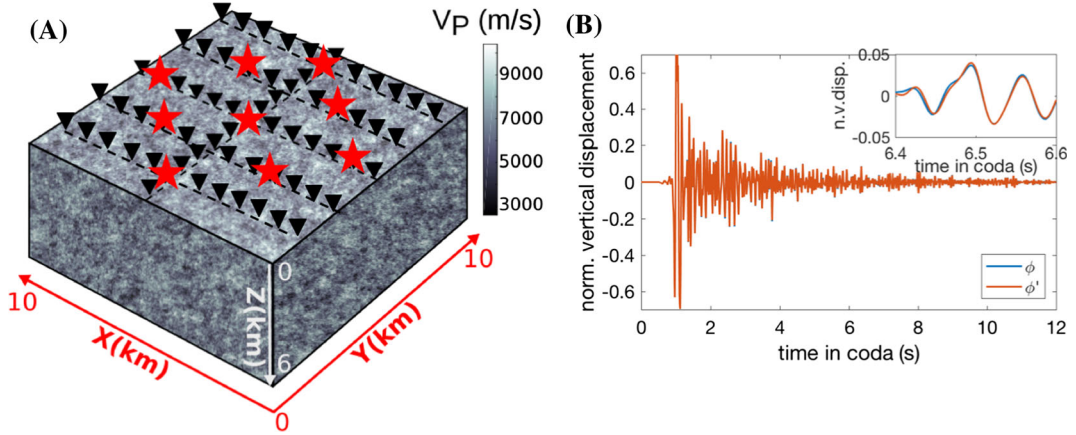


Figure 2

**a** Heterogeneous model  $(x, y) = 10$  km,  $z = 6$  km. The red stars mark the source positions and the black inverted triangles mark some exemplary receiver positions. **b** Synthetic seismograms recorded without ( $\phi$ , blue) and with a velocity perturbation ( $\phi'$ , red) at a 1.5-km depth in a medium with 20% velocity fluctuation

2014b), or stochastic medium characterization (Nakata and Beroza 2015).

For each source setup, the wave field is first simulated in an unperturbed medium. Then, a velocity reduction of 500 m/s ( $\approx 8\%$ ) within a cube of 500-m side and length is introduced at  $(x, y) = 6$  km and  $z = 0.5, 1$ , and 2 km, respectively. The relative phase shifts between both simulations are measured at various lapse times in the coda (2–10 s) using the stretching technique (Lobkis and Weaver 2003; Sens-Schönfelder and Wegler 2006a). The stretching technique is applied in narrow moving time windows of 1 s. These time windows are long enough to estimate a stable waveform distortion at each lapse time. With lapse time, the diffusive halo of the coda waves changes and different parts of the medium are sampled, which affects the measured relative phase shift. The relative phase shift is constant with coda lapse time only when the velocity change is global (i.e. uniformly affecting the medium); if the medium change is local, the relative phase shift with lapse time is non-linear (Obermann et al. 2013b).

### 2.3. Linear Least-Square Inversion Procedure

To estimate the spatial distribution of the velocity changes, we pose the direct problem  $d_i = G_{ij}m_j$ , where  $d_i (i = 1 \dots n)$  is a vector containing the relative

phase shifts that we measured between the  $n$  combinations of receivers and different sources.  $G$  is a matrix for which each component  $G_{ij} = \frac{\Delta V}{t} K_{ij}$  corresponds to the combined sensitivity kernel for the receiver/source pair  $i$  in cell  $j$  evaluated at time  $t$  in the coda and weighted by the volume of the cells  $\Delta v$  and the lapse time  $t$  in the coda.  $m$  is a vector, for which each component  $m_j$  contains the actual relative velocity changes that we estimate for each pixel  $j$  (unitless).

To determine  $m$ , we use the regularized linear least-square method as formulated by Tarantola and Valette (1982):

$$m = m_0 + C_m G^t (G C_m G^t + C_d)^{-1} (d - G m_0), \quad (10)$$

where  $m_0$  is the initial model, a zero vector in our case, as we do not possess any a priori information about the expected changes.  $C_d$  is the diagonal covariance matrix for the data and contains the variances of the data  $\sigma_{d,i}^2$  estimated following Weaver et al. (2011).  $C_m$  is the covariance matrix for the model. To limit the number of independent parameters, we introduce a spatial smoothing obtained from the correlation of neighbouring cells in the covariance matrix of the model  $C_m$  via an exponential function. The elements  $(i, j)$  of the else-wise diagonal matrix are given by:



$$C_m(i,j) = \left(\sigma_m \frac{\lambda_0}{\lambda}\right)^2 \exp\left(-\frac{\delta_{ij}}{\lambda}\right), \quad (11)$$

where  $\delta_{ij}$  is the distance between two cells  $i$  and  $j$ . The matrix is weighted by  $(\sigma_m \frac{\lambda_0}{\lambda})^2$  where  $\lambda_0$  is the scaling factor that was taken here equal to grid discretisation of the combined sensitivity kernels (500 m) and  $\lambda$  is the correlation length that defines the length over which the parameters are correlated.  $\sigma_m$  is the a priori standard deviation of the model.  $\lambda$  and  $\sigma_m$  are determined using the  $L$  curve criterion (Hansen 1992).

We perform this inversion jointly for different times ( $t = 2, 3$ , and  $4$  s) in the coda with the corresponding universal partition ratios ( $\alpha = 0.80, 0.75, 0.69$ ) (Obermann et al. 2014a) of surface- and body-wave sensitivity. The idea behind the joint inversion is that the diffusive halo as well as the contribution of body and surface waves and hence the region sampled by the waves, change with lapse time. A joint inversion of different lapse times will hence help to constrain the depth position of the perturbation. At later times  $> 4$  s, because the energy fills the volume of our model, the imprint of the change is homogeneously spread over a very large area, with little spatial contrast and, thus, no imaging potential with the full space kernels we are using.

### 3. Results from the Numerical Wave-Field Simulations

In Fig. 3, we show cuts of the inverted 3-D velocity change model through the vertical plane (at  $y = 5$  km) corresponding to perturbations introduced at depth of 0.5 km ( $1.5\lambda_p, 2.6\lambda_s$ ), 1 km ( $3\lambda_p, 5\lambda_s$ ) and 2 km ( $6\lambda_p, 10.5\lambda_s$ ). We compare inversions performed with the 3-D combined kernels (first column) with kernels describing body-wave propagation only (second column) and with kernels describing surface wave propagation only (third column). The blue square indicates the location of the cubic velocity perturbation that we want to image.

For all depth positions, the inversions using 3-D combined kernels resolve the spatial locations of the velocity perturbation reasonably well (Fig. 3, first column). For better visualisation, the colour scale is

adjusted to the min./max. values of the retrieved changes. Because we introduce smoothing to regularize the linear inversion method, the imaged velocity changes are extended in space. The retrieved extended but weak velocity changes produce similar phase shifts than the true small but strong velocity changes. Integrating the changes over their spatial extension leads to similar values.

In the second and third column of Fig. 3, we focus on the inversion results using body- and surface-wave sensitivities alone, which corresponds to partition ratios of  $\alpha = 0$  and  $\alpha = 1$ , respectively. While the inversions provide an accurate location in the horizontal plane, except for the inversion using the surface-wave-only kernels at largest depth (lowest subplot in the third column in Fig. 3), these kernels cannot provide a depth estimate of the changes. In our simulations, a significant part of the energy is contained in the surface waves ( $\alpha > 0.6$  at  $t > 2$  s). The body-wave-only kernel can hence not accurately describe the coda-wave sensitivity. Concerning the surface-wave-only kernel, there are several reasons to explain the bad performance. The shallowest perturbation, at 0.5-km depth, is already at  $2.5\lambda_s$ , which is deep for the surface-wave kernel to probe. We also only use results from a single frequency (source with a central frequency at 20 Hz) to describe the surface-wave kernel. Surface waves are dispersive and their sensitivity to changes at depth depends on the period. Shorter periods with short wavelengths are sensitive to shallower changes, while longer periods with longer wavelengths, sample increasing depth ranges (Rivet et al. 2011). Taking a frequency analysis into account, the performance of the surface-wave-only kernel might be improved in settings that are dominated by surface waves and help to locate changes at shallow depth ( $< 1\lambda_s$ ).

In the following, we discuss limitations of the method focussing on physical, as well as practical issues.

Let us focus on the *source/receiver configuration*. In Fig. 4a, b we show horizontal slices through the relative velocity change model close to the surface resulting from a central, cubic velocity perturbation at 2-km depth (blue square). For the simulations in Fig. 4b, we used eight sources distributed along a circle (white crosses). For the simulations in Fig. 4a,

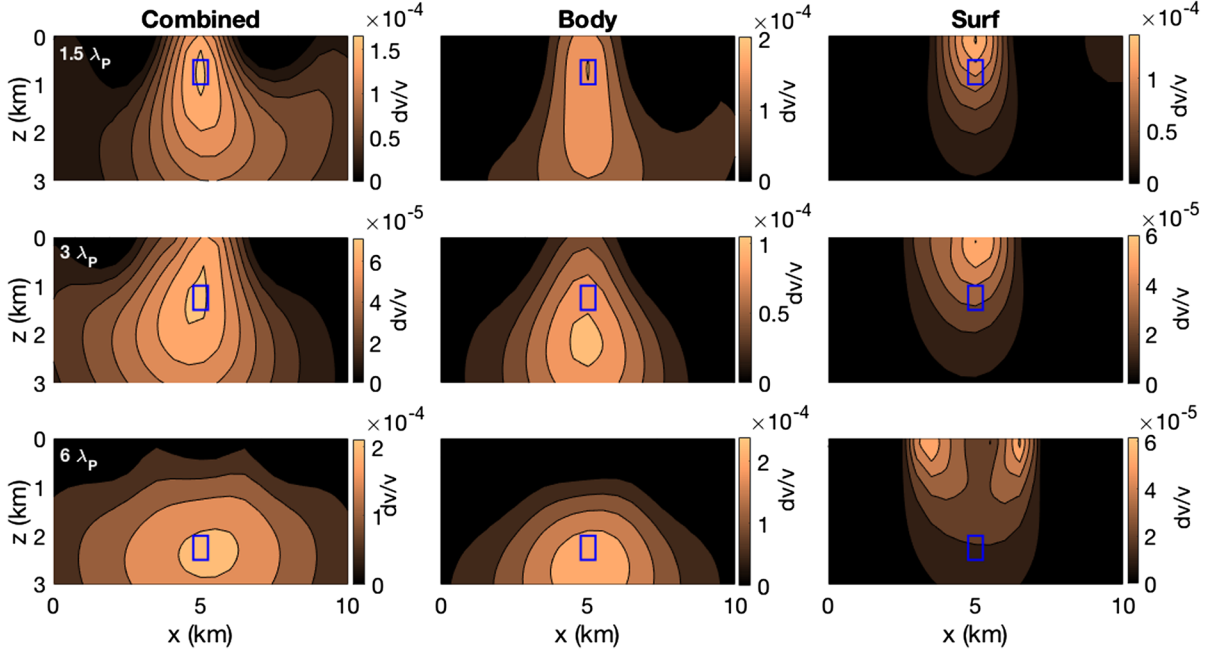


Figure 3

Vertical cuts through the relative velocity change model along  $y = 5$  km. Cubic velocity perturbations (blue square) are placed at depths of 0.5 km (first row), 1 km (second row) and 2 km (third row). The inversions were performed using the 3-D combined kernels (first column), 3-D kernels describing body-wave propagation only (second column) and 2-D kernels describing surface-wave propagation only (third column)

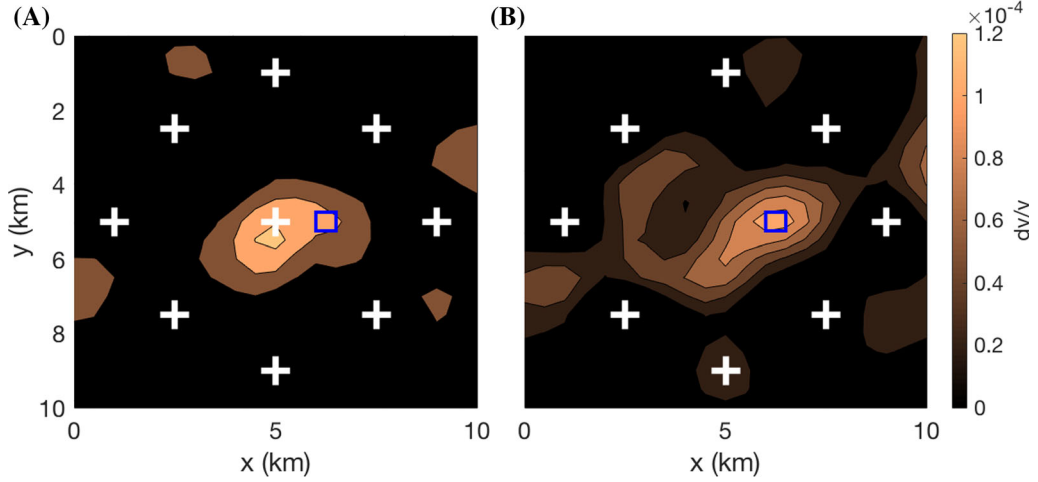


Figure 4

Horizontal cuts through the relative velocity change model close to the surface for a cubic velocity change at 2-km depth. The projection of the location of the velocity change is shown with the blue square. For the simulations, nine (a) and eight (b) sources are used as indicated with the white crosses

we added a ninth source in the centre that is much closer to the location of the velocity perturbation compared to the other sources. Consequently, we

observe that the location of the velocity perturbation, as seen by the inversion, is shifted towards the position of the central source, where the sensitivity



concentrates. A source/receiver too close to the change has a tendency to shift the localisation. A correct estimation of the sensitivity is only possible if the propagation distance/time has been sufficiently large to enter the diffusive regime.

Besides the geometry of the sources and receivers, the inversion is also influenced by the value of the *transport mean free path*  $\ell^*$ . In Fig. 5 we repeat an inversion with a cubic velocity change at 1-km depth using different values of  $\ell^*$  in the computation of the kernels. Obermann et al. (2013a) had tested the sensitivity of the 2-D inversion toward different values of  $\ell^*$  and had observed that  $\ell^*$  has an influence on the size of the affected area but not on the horizontal location itself. While in 3-D, this remains true for the horizontal location, we observe that even a slight inaccuracy in the value of  $\ell^*$  has an effect on the depth location. A too small  $\ell^*$  leads to an underestimation of the perturbation depth, while the opposite leads to an overestimation. The exact value for this set of simulations is  $\ell^* = 1.84$  km.  $\ell^*$  controls the shape of the diffusive halo, including in the vertical direction. On the horizontal plane, the effect is less important as the errors are compensated for by the distribution of the receivers. In our configuration, there are no receivers at depth to help constraint the position of the change in the vertical plane.

Margerin et al. (2016) pointed out that the sensitivity kernels should be based on the *specific intensity* to properly model the effect of a velocity perturbation on the coda waves. Contrary to the (angularly averaged) intensity, the specific intensity depends on the

direction of wave propagation. Taking into account this angular dependency would be important to describe non-diffusive regimes, especially in the case of anisotropic medium scattering. This issue lies beyond the scope of this paper and will be addressed in future works. In this study, we focus on the general construction of the 3-D kernel via a combination of surface- and body-wave sensitivity. In future works, the individual kernels should be updated with the kernels of Margerin et al. (2016). This, however, does not affect the validity of our approach.

#### 4. Application to the $M_w$ 7.9, 2008 Wenchuan Earthquake

In a first attempt to apply the 3-D combined kernels to real data, we chose a passive seismic monitoring application. Obermann et al. (2014a) had previously processed data from a dense network in China that was in operation during the  $M_w$  7.9, 2008 Wenchuan earthquake that struck the Longmen Shan region along the Eastern margin of the Tibetan Plateau (Burchfiel et al. 2008; Zhang et al. 2010).

The earthquake occurred at a depth of about 19 km (Chen et al. 2009) and affected a 240-km-long rupture zone (Xu et al. 2009). A dense network deployed by the Institute of Geology of the China Earthquake Administration covered 2/3 of the fault system activated during the Wenchuan earthquake in 2008. Chen et al. (2010) and Froment et al. (2013) detected time-lapse changes in the coda of the cross-

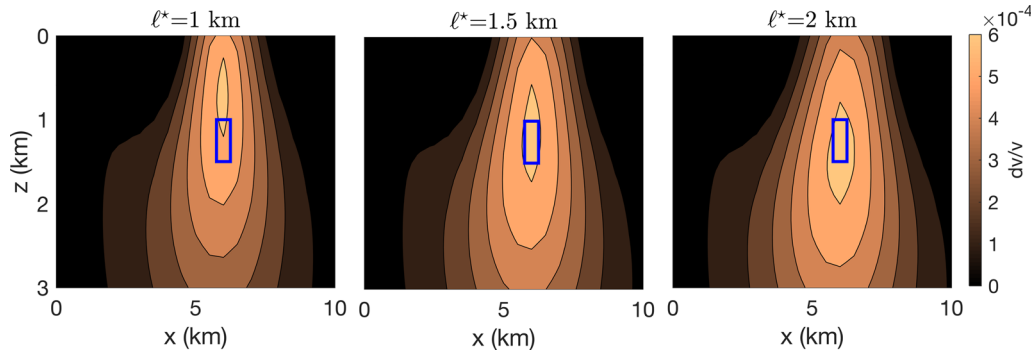


Figure 5

Vertical cuts through the relative velocity change model along  $x = 6$  km for a cubic velocity perturbation at 1 km. For the inversions, we used 3-D combined sensitivity kernels with different scattering mean free paths. The exact value for this set of simulations is  $\ell^* = 1.84$  km

correlations from 156 stations covering the fault system within two different period bands, in which the surface waves are sensitive to shallower (1–3 s) and larger depths (12–20 s). In the period band of 12–20 s, Froment et al. (2013) and Obermann et al. (2014a) could observe a strong post-seismic signature of the middle crust to the earthquake, and also detect a clear seasonal signature of the velocity changes within the Sichuan basin that they related to a loading effect due to the heavy rainfalls during the monsoon season. Obermann et al. (2014a) studied the changes in the 12–20-s period band at different lapse times. The post-seismic change is more prominent at later lapse times, indicating a greater depth, while the change due to the monsoon rain is more prominent at earlier times, indicating a shallower depth. In this region, surface waves in the period band from 12–20 s are estimated to be sensitive to a depth range of 5–40 km (Froment et al. 2013), leaving a wide range for the depth of a relatively ‘shallow’ or ‘deep’ change. Obermann et al. (2014a) used 2-D probabilistic sensitivity kernels to locate the apparent velocity changes at different lapse times on the horizontal plane (Fig. 6a, b). In this previous work, the loading effect of the monsoon rain (a) was constrained to the Sichuan basin and could be clearly separated from the post-seismic signature (b).

In Fig. 6c, d, we show a vertical cross section through the model of velocity perturbation that we obtain from an inversion with the 3-D combined kernels along the red line indicated in Fig. 6a, b. To compute the diffusivity for the kernels, we used an effective velocity of 5 km/s and a transport mean free path of  $\ell^* = 500$  km, which corresponds to the values used for the 2-D inversion by Obermann et al. (2014a). The exact value for  $\ell^*$  in this region in China is not known, but our estimate lies well within the broad range of observed values in these period bands for scattering around the globe (Sato and Nohechi 2001; Lee et al. 2003; Hillers et al. 2013; Sens-Schönfelder and Wegler 2006b).

From the results in Fig. 6c, d, we see that the inversion with the 3-D combined kernels allows us to constrain the depth of the changes. The peak velocity reduction in the Sichuan basin is constrained to the upper 15 km of the crust. This strengthens our interpretation that the velocity change is due to a

loading effect of the rain and not related to water infiltration, which cannot reach such depths. Loading can significantly increase the pore pressure (Bettinelli et al. 2008) and reduce the velocity (Dvorkin et al. 1999; Carcione and Tinivella 2001).

The maximal velocity reduction in the month following the Wenchuan earthquake is constrained to 20–30 km of depth. As pointed out by Froment et al. (2013) and Obermann et al. (2014a), no co-seismic velocity reduction in this period range (12–20 s) could be observed. Given the depth range, the observed changes might have been caused by earthquake-related processes at depth (after-slip, viscoelastic response, fluid transfer, etc.). Specifically, the slip of a deep decollement beneath Eastern Tibet as an aftereffect of the Wenchuan earthquake has been proposed by Fielding et al. (2013) and Obermann et al. (2014a).

## 5. Conclusion

We have shown that it is possible to constrain the depth of medium changes in multiply scattered media with an imaging procedure that involves a linear combination of body- and surface-wave sensitivity kernels. We have seen that the accuracy of the location results depends on the geometry of the sources and receivers, and the accurate characterisation of the subsurface scattering. A limitation for real data applications is that the scattering properties of the subsurface are often poorly constrained. We show a promising first application of the kernels to locate velocity changes at depth that were obtained from the correlations of ambient seismic noise data covering the region affected by the 2008 Wenchuan earthquake. Constraining the depth location of the changes can significantly improve our understanding of the nature of the medium variations revealed by seismic monitoring. As standard methods are not effective to provide images of the texture of the rock at depth (e.g. small-scale heterogeneities, cracks, voids), we think that new imaging approaches that make use of multiply scattered and sensitive coda waves can help to make progress in this direction. Following the presented approach, an improvement should be done on the level of the individual kernels (2-D surface and

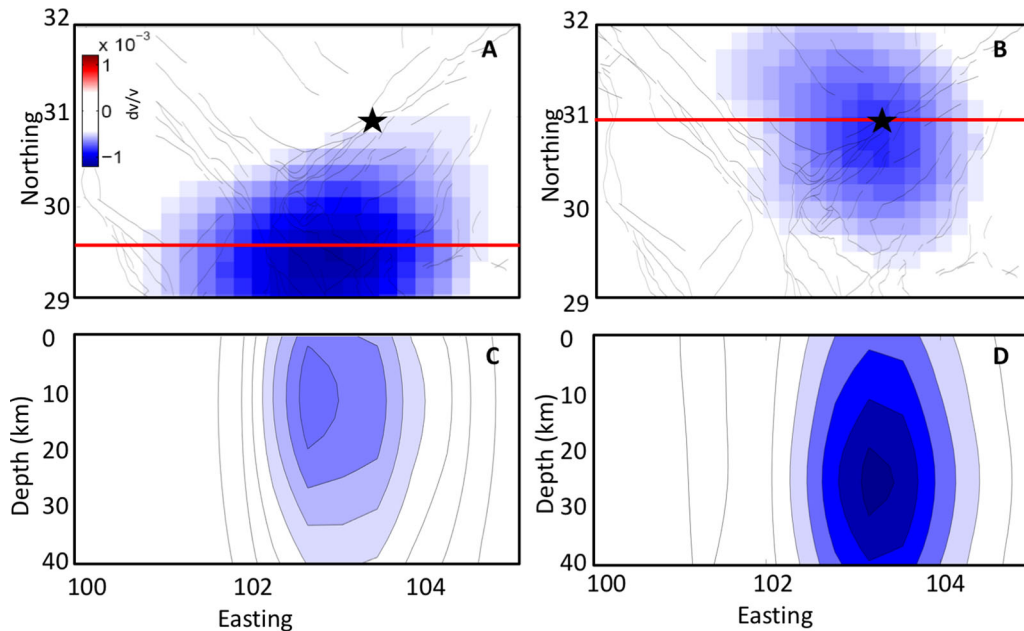


Figure 6

Inversion results on the horizontal plane of the apparent velocity model in the Sichuan region after the  $M_w$  7.9, 2008 Wenchuan earthquake (star) at 50 s in the coda **a** featuring the loading effect due to the monsoon rain and at 90 s in the coda **b** featuring the post-seismic effects (modified from Obermann et al. (2014a)). The vertical cuts (**c**, **d**) along the red line indicated in **a** and **b** were computed with the 3-D combined kernels

3-D body) to account for the directionality of the energy flux and address non-diffusive regimes.

manuscript, as well as the editor Yehuda Ben-Zion for his helpful suggestions.

### Acknowledgements

The research leading to these results received funding from the European Community Seventh Framework Programme under grant agreement no. 608553 (Image) and the Swiss Federal Office of Energy with the project GEOBEST. The authors also want to thank the Leibniz-Rechenzentrum (LRZ) and Jens Oeser for access and support in using the SUPER-MUC system at the LRZ. The work has benefited from discussions within the European Cooperation in Science and Technology (COST) action ES1401-TIDES, supported by COST. MC acknowledges the support of the European Research Council (ERC) under agreement no. 742335 (F-Image). The authors wish to thank Gregor Hillers and an anonymous reviewer for their very constructive and detailed comments that helped to significantly improve the

### REFERENCES

- Bettinelli, P., Avouac, J. P., Flouzat, M., Bollinger, L., Ramillien, G., Rajaure, S., et al. (2008). Seasonal variations of seismicity and geodetic strain in the Himalaya induced by surface hydrology. *Earth and Planetary Science Letters*, 266, 332–344.
- Burchfiel, B. C., Royden, L. H., van der Hilst, R. D., Chen, Z., King, R. W., Li, C., et al. (2008). A geological and geophysical context for the Wenchuan earthquake of 12 May 2008, Sichuan, People's Republic of China. *GSA Today*, 18(7), 5.
- Carcione, J. M., & Tinivella, U. (2001). The seismic response to overpressure: A modelling study based on laboratory, well and seismic data. *Geophysical Prospecting*, 49, 523–539.
- Chen, J. H., Froment, B., Liu, Q. Y., & Campillo, M. (2010). Distribution of seismic wave speed changes associated with the 12 May 2008  $M_w$  7.9 Wenchuan earthquake. *Geophysical Research Letters*, 37(L18302), 1–4.
- Chen, J. H., Liu, Q. Y., Li, S. C., Guo, B., Wang, J., & Qi, S. H. (2009). Seismotectonic study by relocation of the Wenchuan  $M(S)8.0$  earthquake sequence. *Chinese Journal of Geophysics-Chinese Edition*, 52(2), 390–397.
- Dvorkin, J., Mavko, G., & Nur, A. (1999). Overpressure detection from compressional- and shear-wave data. *Geophysical Research Letters*, 26(22), 3417–3420.

- Fielding, E. J., Sladen, A., Li, Z., Avouac, J.-P., Bürgmann, R., & Ryder, I. (2013). Kinematic fault slip evolution source models of the 2008 M<sub>7.9</sub> Wenchuan earthquake in China from SAR interferometry, GPS and teleseismic analysis and implications for Longmen Shan tectonics. *Geophysical journal international*, 194(2), 1138–1166.
- Froment, B. (2011). *Utilisation du bruit sismique ambiant dans le suivi temporel de structures géologiques*. PhD thesis, Université de Grenoble.
- Froment, B., Campillo, M., Chen, J. H., & Liu, Q. Y. (2013). Deformation at depth associated with the May 12, 2008 M<sub>w</sub> 7.9 Wenchuan earthquake from seismic ambient noise monitoring. *Geophysical Research Letters*, 40, 78–82.
- Grêt, A., Snieder, R., Aster, R. C., & Kyle, P. R. (2005). Monitoring rapid temporal change in a volcano with coda wave interferometry. *Geophysical Research Letters*, 32(6), L06304.
- Hansen, P. C. (1992). Analysis of discrete ill-posed problems by means of the L-curve. *SIAM Review*, 34(4), 561–580.
- Hennino, R., Tregoures, N., Shapiro, N. M., Margerin, L., Campillo, M., van Tiggelen, B. A., et al. (2001). Observation of equipartition of seismic waves. *Physical Review Letters*, 86(15), 3447–3450.
- Hillers, G., Ben-Zion, Y., Landes, M., & Campillo, M. (2013). Interaction of microseisms with crustal heterogeneity: A case study from the San Jacinto fault zone area. *Geochemistry, Geophysics, Geosystems*, 14(7), 2182–2197.
- Hillers, G., Husen, S., Obermann, A., Planès, T., Campillo, M., & Larose, E. (2015). Noise-based monitoring and imaging of aseismic transient deformation induced by the 2006 Basel reservoir stimulation. *Geophysics*, 80(4), KS51–KS68.
- Kanu, C., & Snieder, R. (2015a). Numerical computation of the sensitivity kernel for monitoring weak changes with multiply scattered acoustic waves. *Geophysical Journal International*, 203(3), 1923–1936.
- Kanu, C., & Snieder, R. (2015b). Time-lapse imaging of a localized weak change with multiply scattered waves using numerical-based sensitivity kernel. *Journal of Geophysical Research: Solid Earth*, 120(8), 5595–5605.
- Komatitsch, D., & Tromp, J. (2002). Spectral-element simulations of global seismic wave propagation II. Three-dimensional models, oceans, rotation and self-gravitation. *Geophysical Journal International*, 150(1), 303–318.
- Larose, E., Obermann, A., Digulescu, A., Planès, T., Chaix, J. F., Mazerolle, F., et al. (2015). Locating and characterizing a crack in concrete with LOCADIFF: A four-point bending test. *The Journal of the Acoustical Society of America*, 138(1), 232–241.
- Larose, E., Planès, T., Rossetto, V., & Margerin, L. (2010). Locating a small change in a multiple scattering environment. *Applied Physics Letters*, 96(204101), 1–3.
- Lee, W. S., Sato, H., & Lee, K. (2003). Estimation of S-wave scattering coefficient in the mantle from envelope characteristics before and after the ScS arrival. *Geophysical Research Letters*, 30(24), 2248–2252.
- Lesage, P., Reyes-Dávila, G., & Arámbula-Mendoza, R. (2014). Large tectonic earthquakes induce sharp temporary decreases in seismic velocity in Volcán de Colima, Mexico. *Journal of Geophysical Research: Solid Earth*, 119(5), 4360–4376.
- Lobkis, O. I., & Weaver, R. L. (2003). Coda-wave interferometry in finite solids: Recovery of P-to-S conversion rates in an elastodynamic billiard. *Physical Review Letters*, 90(254302), 1–4.
- Margerin, L., Campillo, M., Shapiro, N. M., & van Tiggelen, B. (1999). Residence time of diffuse waves in the crust and the physical interpretation of coda Q. Application to seismograms recorded in Mexico. *Geophysical Journal International*, 138, 343–352.
- Margerin, L., Planès, T., Mayor, J., & Calvet, M. (2016). Sensitivity kernels for coda-wave interferometry and scattering tomography: Theory and numerical evaluation in two-dimensional anisotropically scattering media. *Geophysical Journal International*, 204(1), 650–666.
- Meunier, J., Hugué, F., & Meynier, P. (2001). Reservoir monitoring using permanent sources and vertical receiver antennae The Céré-la-Ronde case study. *The Leading Edge*, 20(6), 622–629.
- Nakahara, H., & Carcolé, E. (2010). Maximum-likelihood method for estimating coda Q and the Nakagami-m parameter. *Bulletin of the Seismological Society of America*, 100(6), 3174–3182.
- Nakata, N., & Beroza, G. C. (2015). Stochastic characterization of mesoscale seismic velocity heterogeneity in Long Beach, California. *Geophysical Journal International*, 203(3), 2049–2054.
- Obermann, A., Froment, B., Campillo, M., Larose, E., Planès, T., Valette, B., et al. (2014). Seismic noise correlations to image structural and mechanical changes associated with the M<sub>w</sub> 7.9 2008 Wenchuan earthquake. *Journal of Geophysical Research*, 119(4), 3155–3168.
- Obermann, A., Kraft, T., Larose, E., Wiemer, S., et al. (2015). Potential of ambient seismic noise techniques to monitor the St. Gallen geothermal site (Switzerland). *Journal of Geophysical Research*, 120(6), 4301–4316.
- Obermann, A., Larose, E., Margerin, L., & Rossetto, V. (2014b). Measuring the scattering mean free path of Rayleigh waves on a volcano from spatial phase decoherence. *Geophysical Journal International*, 197, 435–442.
- Obermann, A., Planès, T., Hadzioannou, C., & Campillo, M. (2016). Lapse-time-dependent coda-wave depth sensitivity to local velocity perturbations in 3-D heterogeneous elastic media. *Geophysical Journal International*, 207(1), 59–66.
- Obermann, A., Planès, T., Larose, E., & Campillo, M. (2013a). Imaging pre- and co-eruptive structural and mechanical changes on a volcano with ambient seismic noise. *Journal of Geophysical Research*, 118(12), 6285–6294.
- Obermann, A., Planès, T., Larose, E., Sens-Schönfelder, C., & Campillo, M. (2013b). Depth sensitivity of seismic coda waves to velocity perturbations in an elastic heterogeneous medium. *Geophysical Journal International*, 194(1), 372–382.
- Paasschens, J. C. J. (1997). Solution of the time-dependent Boltzmann equation. *Physical Review E*, 56(1), 1135.
- Pacheco, C., & Snieder, R. (2005). Time-lapse travel time change of multiply scattered acoustic waves. *The Journal of the Acoustical Society of America*, 118, 1300–1310.
- Peng, Z., & Ben-Zion, Y. (2006). Temporal changes of shallow seismic velocity around the Karadere–Düzce branch of the north Anatolian fault and strong ground motion. *Pure and Applied Geophysics*, 163(2–3), 567–600.
- Perton, M., Sánchez-Sesma, F., Rodríguez-Castellanos, A., Campillo, M., & Weaver, R. (2009). Two perspectives on equipartition in diffuse elastic fields in three dimensions. *The Journal of the Acoustical Society of America*, 126(3), 1125–1130.
- Peter, D., Komatitsch, D., Luo, Y., Martin, R., Le Goff, N., Casarotti, E., et al. (2011). Forward and adjoint simulations of

- seismic wave propagation on fully unstructured hexahedral meshes. *Geophysical Journal International*, 186(2), 721–739.
- Planès, T. (2013). *Imagerie de changements locaux en régime de diffusion multiple*. PhD thesis, Université de Grenoble.
- Planès, T., Larose, E., Margerin, L., Rossetto, V., & Sens-Schönfelder, C. (2014). Decorrelation and phase-shift of coda waves induced by local changes: Multiple scattering approach and numerical validation. *Waves in Random and Complex Media*, 2(24), 1–27.
- Planès, T., Larose, E., Rossetto, V., & Margerin, L. (2015). Imaging multiple local changes in heterogeneous media with diffuse waves. *The Journal of the Acoustical Society of America*, 137(2), 660–667.
- Poupinet, G., Ellsworth, W. L., & Frechet, J. (1984). Monitoring velocity variations in the crust using earthquake doublets: An application to the Calaveras fault. *California Journal of Geophysical Research*, 89(B7), 5719–5731.
- Poupinet, G., Ratdomopurbo, A., & Coutant, O. (1996). On the use of earthquake multiplets to study fractures and the temporal evolution of an active volcano. *Annals of Geophysics*, 39, 253–264.
- Rivet, D., Campillo, M., Shapiro, N. M., Cruz-Atienza, V., Radiguet, M., Cotte, N., et al. (2011). Seismic evidence of nonlinear crustal deformation during a large slow slip event in Mexico. *Geophysical Research Letters*, 38(L08308), 1–5.
- Rossetto, V., Margerin, L., Planès, T., & Larose, E. (2011). Locating a weak change using diffuse waves: Theoretical approach and inversion procedure. *Journal of Applied Physics*, 109(034903), 1–11.
- Roux, P., & Ben-Zion, Y. (2014). Monitoring fault zone environments with correlations of earthquake waveforms. *Geophysical Journal International*, 196(2), 1073–1081.
- Sanchez, P., Obermann, A., Schimmel, M., et al. (2018). Detecting and locating precursory signals during the 2011 El Hierro, Canary Islands, submarine eruption. *Geophysical Research Letters*. <https://doi.org/10.1029/2018GL079550>.
- Sato, H., & Nohechi, M. (2001). Envelope formation of long-period Rayleigh waves in vertical component seismograms: Single isotropic scattering model. *Journal of Geophysical Research: Solid Earth*, 106(B4), 6589–6594.
- Schaff, D. P., & Beroza, G. C. (2004). Coseismic and postseismic velocity changes measured by repeating earthquakes. *Journal of Geophysical Research*, 109(B10302), 1–14.
- Sens-Schönfelder, C., & Wegler, U. (2006a). Passive image interferometry and seasonal variations of seismic velocities at Merapi Volcano. *Indonesia. Geophysical Research Letters*, 33(21), L21302.
- Sens-Schönfelder, C., & Wegler, U. (2006b). Radiative transfer theory for estimation of the seismic moment. *Geophysical Journal International*, 167(3), 1363–1372.
- Takagi, R., Okada, T., Nakahara, H., Umino, N., & Hasegawa, A. (2012). Coseismic velocity change in and around the focal region of the 2008 Iwate-Miyagi Nairiku earthquake. *Journal of Geophysical Research*, 117(B06315), 1–19.
- Tarantola, A., & Valette, B. (1982). Generalized nonlinear inverse problems solved using the least squares criterion. *Reviews of Geophysics*, 20(2), 219–232.
- Tregouères, N. P., & van Tiggelen, B. A. (2002). Generalized diffusion equation for multiply scattered elastic waves. *Waves in Random Media*, 12, 21–38.
- Ugalde, A., Villaseñor, A., Gaite, B., Casquero, S., Martí, D., Calahorrano, A., et al. (2013). Passive seismic monitoring of an experimental CO<sub>2</sub> geological storage site in Hontomín (Northern Spain). *Seismological Research Letters*, 84(1), 75–84.
- Weaver, R. L. (1982). On diffuse waves in solid media. *The Journal of the Acoustical Society of America*, 71, 1608–1609.
- Weaver, R. L. (1985). Diffuse elastic waves at a free surface. *The Journal of the Acoustical Society of America*, 78, 131–136.
- Weaver, R. L., Hadziioannou, C., Larose, E., & Campillo, M. (2011). On the precision of noise correlation interferometry. *Geophysical Journal International*, 185(3), 1384–1392.
- Wu, C., Peng, Z., & Ben-Zion, Y. (2009). Non-linearity and temporal changes of fault zone site response associated with strong ground motion. *Geophysical Journal International*, 176(1), 265–278.
- Xu, X. W., Wen, X. Z., Yu, G. H., Chen, G. H., Klinger, Y., Hubbard, J., et al. (2009). Coseismic reverse- and oblique-slip surface faulting generated by the 2008  $M_w$  7.9 Wenchuan earthquake, China. *Geology*, 37(6), 515–518.
- Zhang, P. Z., Wen, X. Z., Shen, Z. K., & Chen, J. H. (2010). Oblique, high-angle, listric-reverse faulting and associated development of strain: The Wenchuan earthquake of May 12, 2008, Sichuan, China. *Annual Review of Earth and Planetary Sciences*, 38, 353–382.
- Zhang, Y., Planès, T., Larose, E., Obermann, A., Rospars, C., & Moreau, G. (2016). Diffuse ultrasound monitoring of stress and damage development on a 15-ton concrete beam. *The Journal of the Acoustical Society of America*, 139(4), 1691–1701.

(Received May 2, 2018, revised September 30, 2018, accepted October 4, 2018)